# Dark solitons in Fabry-Pérot resonators with Kerr media and normal dispersion

Graeme N. Campbell,[1,2,*] Lewis Hill,[1,2] Pascal Del'Haye,[2,3] and Gian-Luca Oppo[1]
[1]*SUPA and Department of Physics, University of Strathclyde, Glasgow G4 0NG, Scotland, United Kingdom*
[2]*Max Planck Institute for the Science of Light, 91058 Erlangen, Germany*
[3]*Department of Physics, Friedrich Alexander University Erlangen-Nuremberg, 91058 Erlangen, Germany*

(Received 7 June 2023; accepted 28 August 2023; published 8 September 2023)

The ranges of existence and stability of dark cavity-soliton stationary states in a Fabry-Pérot resonator with a Kerr nonlinear medium and normal dispersion are determined. The Fabry-Pérot configuration introduces nonlocal coupling that shifts the cavity detuning by the round trip average power of the intracavity field. When compared with ring resonators described by the Lugiato-Lefever equation, nonlocal coupling leads to strongly detuned dark cavity solitons that exist over a wide range of detunings. This shift is a consequence of the counterpropagation of intracavity fields inherent to Fabry-Pérot resonators. In contrast with ring resonators, the existence and stability of dark soliton solutions are dependent on the size and number of solitons in the cavity. We investigate the effect of nonlocal coupling of Fabry-Pérot resonators on multiple dark solitons, and we demonstrate long-range interactions and synchronization of temporal oscillations.

DOI: 10.1103/PhysRevA.108.033505

## I. INTRODUCTION

Temporal cavity solitons (TCSs) [1] have attracted significant interest for the generation of broadband optical frequency combs [2], with many applications in telecommunication [3,4], spectroscopy [5,6], and in the fundamental studies of complex dissipative structures. TCSs in high-$Q$ ring microresonators are now routinely used to produce frequency combs. Light propagation in microring resonators is well described by the longitudinal version of the Lugiato-Lefever equation (LLE) [7]. The LLE originally described the transverse, dissipative spatial structures in passive optical systems with diffraction, and it was later adapted to describe pattern formation along the cavity length [8,9].

In recent years, the generation of bright TCSs within Fabry-Pérot (FP) resonators in the anomalous dispersion regime was first studied analytically [10,11] and then experimentally demonstrated for continuous wave [12] and pulsed [13] driving. The generation of frequency combs produced by modulational instabilities and Turing patterns in FP resonators has also been demonstrated [14]. This has resulted in increasing interest in linear resonators for the generation of TCSs as the FP geometry can offer additional engineering possibilities when compared to a ring resonator for tailoring dispersion and allowing for greater control over the bandwidth and temporal duration of cavity solitons. Such possibilities include the engineering of the core-cladding index [15], analogous to the engineering of ring resonator geometry, or the design of the mirror dispersion [12].

Here we extend the work of Ref. [10] to the case of normal dispersion where stable dark cavity solitons (DCSs) are found as opposed to bright ones. We model a FP resonator filled with a Kerr nonlinear medium and investigate the inherent counterpropagation of light under normal dispersion in Sec. II. In Sec. III, we describe first how the FP configuration results in many unstable stationary solutions, which are stable in an equivalent ring resonator. In spite of this fact, solutions containing moving fronts between bistable states (plateaus) exist and are described in Sec. IV. It is these moving fronts that can lock with each other and form DCS solutions as discussed in Sec. V. Since one of these local structures can exist within the cavity, it is preferential to label these as cavity solitons even in regimes when they may form trains of pulses. This is in agreement with the laser case [16]. DCS stationary solutions are found to be detuning shifted with respect to those in a ring resonator described by the LLE by the average power of the field over a round trip of the cavity. This is a result of an additional nonlocal coupling term exhibited by the FP resulting from counterpropagation of the intracavity fields. To properly elucidate the effects of the shift in detuning, stationary solutions of the FP model and their stability are compared with those of ring resonators with normal dispersion [17,18], those of FP with anomalous dispersion [10], and those of counterpropagating light in ring resonators with normal dispersion [19]. Finally we investigate in Sec. VI oscillatory DCS solutions in a FP, and we discuss the effects of nonlocal coupling on the oscillating solitons, the homogeneous background, and the interaction of two oscillating DCSs. In particular, the long-range interaction between DCSs is capable of synchronizing their oscillations.

We note that dark and bright solitons as well as plateau solutions have also been discussed in time-delayed Gires-Tournois interferometers formed by a FP cavity and external mirrors [20,21].

*graeme.campbell.2019@uni.strath.ac.uk

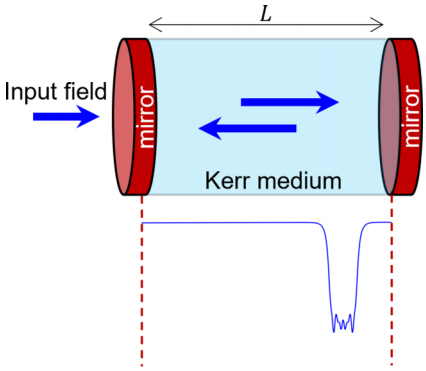


FIG. 1. Setup: A Fabry-Pérot resonator filled with a Kerr medium. An input field pump enters the cavity on one side and part of the field is coupled out upon each reflection at the output mirror. An example field power displaying a DCS is shown.

## II. THE FABRY-PÉROT MODEL

We consider a high finesse FP resonator composed of highly reflective mirrors and filled with a Kerr medium; see Fig. 1. The resonator is driven by linearly polarized light, which is coupled through one of the cavity mirrors into the resonator, and the intracavity field is coupled out upon each reflection. This system was previously studied in the case of anomalous dispersion in [10], where a so-called Lugiato-Lefever equation for the Fabry-Pérot (FP-LLE) was derived. For normal dispersion, the dimensionless FP-LLE has the form

$$\partial_t \psi = S - (1 + i\theta)\psi + i(|\psi|^2 + 2\langle|\psi|^2\rangle)\psi - i\partial_\zeta^2 \psi, \quad (1)$$

where $\psi(\zeta, t)$ is an auxiliary field of slowly varying amplitudes defined (see below) over the extended domain $-L \leqslant \zeta \leqslant L$ with periodic boundary conditions, $L$ is the resonator length, $S$ is the amplitude of the normalized input field, which is considered to be real and positive, and $\theta$ is the normalized detuning to the near nearest cavity resonance. Here, $t$ is the "slow time" temporal variable describing the evolution over many round trips of the cavity, while $\zeta$ is the "fast time" longitudinal variable describing the evolution over a single round trip of the linear cavity. This formulation allows us to clearly compare the FP results with those of a ring resonator configuration as is discussed throughout this paper. As shown in [10], the auxiliary field $\psi$ in Eq. (1) is related to the slowly varying field envelopes of the forward, $F(\zeta, t)$, and backward, $B(\zeta, t)$, counterpropagating fields via

$$F(\zeta, t) = \sum_{\mu=-\infty}^{+\infty} f_\mu(t) e^{-i\alpha_\mu(t - \frac{\zeta}{v_g})}, \quad (2)$$

$$B(\zeta, t) = \sum_{\mu=-\infty}^{+\infty} f_\mu(t) e^{-i\alpha_\mu(t + \frac{\zeta}{v_g})} \quad (3)$$

over the domain $0 \leqslant \zeta \leqslant L$, where the modal coefficients, $f_\mu$, are defined as

$$f_\mu(t) = \frac{1}{2L} \int_{-L}^{L} d\zeta e^{-i\frac{\alpha_\mu}{v_g}\zeta} \psi(\zeta, t) \quad (4)$$

with $\alpha_\mu = \pi\mu v_g/L$, group velocity $v_g$, and mode number $\mu$. As in [10], Eq. (1) was obtained under the conditions of a large material detuning, a high-$Q$ cavity, negligible higher-order dispersion, slowly varying amplitude, and Kerr-cubic approximations. The term notated with angled brackets in Eq. (1) represents the integral

$$\langle|\psi|^2\rangle = \frac{1}{2L} \int_{-L}^{L} |\psi|^2 d\zeta \quad (5)$$

corresponding to the average power of the intracavity field over a round trip of the resonator. This term arises due to the counterpropagation of the fields, which is inherent in a FP configuration. Integral terms of this kind are also present in bidirectionally pumped ring resonators where instead there are two coupled equations, one for each counterpropagating field [19,22,23], and they are the result of rapid phase dynamics of cross-coupling terms due to the fields seeing each other through an average intensity.

A connection between Eq. (1) and a LLE for a ring resonator system was previously made in [10] and investigated in the context of anomalous dispersion. By writing Eq. (1) as

$$\partial_t \psi = S - (1 + i\theta_{\text{eff}})\psi + i|\psi|^2\psi - i\partial_\zeta^2 \psi, \quad (6)$$

we can see that the stationary solutions of Eq. (1) are also stationary solutions of the LLE with an identical input field $S$ and an effective detuning

$$\theta_{\text{eff}} = \theta - 2\langle|\psi|^2\rangle \quad (7)$$

that is shifted by the average power of the intracavity field. The role of this effective detuning in counterpropagation in a ring resonator was investigated in [19]. The shift in detuning introduced by the FP configuration results in distinct features of the TCSs as discussed in the following sections.

## III. HOMOGENEOUS STATES AND PLATEAUS

We describe stationary solutions composed of flat increments over the cavity round trip of the FP model in the fast time, the normalized longitudinal coordinate $\zeta$. We write Eq. (1) for $\partial_t \psi = 0$ as

$$\begin{aligned} &\partial_\zeta U = \tilde{V}, \quad \partial_\zeta V = \tilde{U}, \\ &\partial_\zeta \tilde{U} = -(\theta - \langle U^2 + V^2\rangle)U - V + UV^2 + U^3, \\ &\partial_\zeta \tilde{V} = -(\theta - \langle U^2 + V^2\rangle)V + U + VU^2 + V^3 - S, \end{aligned} \quad (8)$$

where $U, V$ are the real and imaginary components of $\psi$. We consider the system of Eq. (8) to evolve in fast time $\zeta$ over a round trip of the cavity, and we adopt the terminology of [17,24–27]. Under this construction, the fixed points $U_0, V_0$ of Eq. (8) correspond to $\partial_\zeta U = \partial_\zeta V = \partial_\zeta \tilde{U} = \partial_\zeta \tilde{V} = 0$. Due to the presence of the nonlocal terms, the fixed points of Eq. (8) depend on the round-trip average power of the field and require the full evolution over the round trip of the resonator for their determination. Fixed points corresponding to homogeneous stationary states (HSSs) satisfy $\langle|\psi_s|^2\rangle = |\psi_s|^2$ and can be found by solving (see [10,28])

$$H^3 - 2(\theta - 2H)H^2 + \{(\theta - 2H)^2 + 1\}H = S^2, \quad (9)$$

where $H^2 = |\psi_s|^2 = \langle|\psi_s|^2\rangle$.

The linear stability analysis of the FP HSSs can be found in Ref. [10] showing that the middle power HSS in the simultaneous presence of three HSSs is always unstable. A more

general discussion on the instabilities of the FP resonators is given in [29]. The HSSs are fixed points of Eq. (8) when the average power over the round trip is equal to the fixed point power. As such, it is not possible for solutions that start and return to a homogeneous state (including front and DCS solutions; see Secs. IV and V) to hang from the HSSs as the presence of a nonlocal fast time inhomogeneity would change the average power of the field. Hence the HSSs of the FP model are a subset of fixed points that do not support exponentially localized solutions.

We consider now the fixed points of Eq. (8) corresponding to homogeneous plateaus connected by step functions. These plateau states have uniform power $Y_\pm$ of finite size $1-\Delta$ and $\Delta$, respectively, in the normalized fast time variable $\zeta/(2L)$, and they are then different from the HSSs. The round-trip average power is given by $\langle|\psi|^2\rangle = \Delta Y_- + (1-\Delta)Y_+$ parametrized by the two bistable plateau powers and the plateau durations with $0<\Delta<1$. The plateau powers are then the solutions of the coupled cubic equations

$$Y_\pm^3 - 2[\theta - 2\Delta Y_- - 2(1-\Delta)Y_+]Y_\pm^2 + \{[\theta - 2\Delta Y_- - 2(1-\Delta)Y_+]^2 + 1\}Y_\pm = S^2. \quad (10)$$

For each value of the plateau duration $\Delta$, there are up to nine possible solutions. When restraining to real solutions that satisfy $Y_+ > Y_-$, at most three pairs of $(Y_+, Y_-)$ solutions remain. For each of these pairs, one can evaluate the effective detuning and find that only one pair corresponds to the upper-lower HSS of the corresponding LLE, if these exist. In this way, one obtains two plateau powers for each value of $\Delta$ unless the effective detuning is outside the bistability region of the corresponding LLE. This approximation has been used to great effectiveness to describe and predict stable switching fronts between plateaus in bidirectionally pumped ring resonators [19]. We will see in Sec. IV that solutions of a plateau connected by switching fronts are dynamical for the FP model while they have large ranges of stability in bidirectional ring resonators.

If we consider perturbations that preserve the average power of the intracavity field $\psi$, the fast time stability of the plateau states can be understood by considering the Jacobian matrix

$$J = \begin{pmatrix} 0 & 0 & 1 & 0 \\ 0 & 0 & 0 & 1 \\ V^2 + 3U^2 - \theta_{\rm eff} & -1 + 2UV & 0 & 0 \\ 1 + 2UV & U^2 + 3V^2 - \theta_{\rm eff} & 0 & 0 \end{pmatrix}_{(U_s, V_s)}, \quad (11)$$

where $U_s$ and $V_s$ are the steady states of Eqs. (8), and $\theta_{\rm eff}$ is the effective detuning corresponding to the stationary field. We note that the Jacobian matrix assumes negligible change to the round-trip average power and provides eigenvalues of the form

$$\lambda = \pm\sqrt{(2Y - \theta_{\rm eff}) \pm \sqrt{(Y^2-1)}}, \quad (12)$$

where $Y = U_0^2 + V_0^2$ is the plateau power of the stationary state $U_s, V_s$ from Eq. (8). The Jacobian (11) has a similar form to the fast time analysis performed for a LLE [17], where $\theta$ replaces the effective detuning and the plateaus correspond to the HSS. The eigenvalues of Eq. (12) rule the escape from and the approach to plateau states $Y_\pm$ along the stable and unstable manifolds. Of key relevance is the transition that occurs at plateau power $Y = 1$, below which the eigenvalues of Eq. (12) become complex. The lower power plateau typically exists beneath this threshold, $Y_- < 1$, displaying fast time oscillation. This allows for the structurally stable intersection of stable and unstable manifolds of the plateau corresponding to the formation of dark cavity solitons [30]. These eigenvalues are essential in the determination of the presence of local oscillations responsible for the existence and stability of dark cavity solitons in Sec. V. We note that the higher power plateau always has power $Y_+ > 1$ and yields four real eigenvalues for the parameters we have considered.

### A. Plateau stability in the slow time

The linear stability of the HSS of the FP has been been previously explored [10], but due to the presence of the round-trip average term in Eq. (1) the existence and linear stability of a plateau solution depends now on the full field variable along $\zeta$. Here we investigate the linear stability in the slow time of solutions $\psi = \psi_+ + \psi_-$ formed by two plateaus $\psi_\pm$, coexisting on a round trip and joined by two step functions in fast time separated by the distance $\Delta$. We determine the linear stability of these solutions to perturbations of the form

$$\psi_\pm = \psi_{\pm,s} + (\epsilon_\pm e^{ik_\pm\zeta + \Omega_\pm t} + \text{c.c.}), \quad (13)$$

where $\epsilon_\pm \ll 1$ while $k_\pm$ and $\Omega_\pm$ are fast-time wave numbers and slow-time frequencies on the corresponding plateau $\pm$. In the case of $k_-\Delta L > \pi$ and $k_+(1-\Delta)L > \pi$, the effect of these perturbations on the round-trip average becomes $\langle|\psi_s + \epsilon|^2\rangle = \langle|\psi_s|^2\rangle$, and we find that the growth rates of the perturbation on the higher power $\Omega_+$ and lower power $\Omega_-$ plateaus are

$$\Omega_+ = -1 \pm \sqrt{4Y_+\theta_{\rm eff} - 3Y_+^2\theta_{\rm eff}^2 - (4Y_+ - \theta_{\rm eff})k_+^2 - k_+^4},$$
$$\Omega_- = -1 \pm \sqrt{4Y_-\theta_{\rm eff} - 3Y_-^2\theta_{\rm eff}^2 - (4Y_- - \theta_{\rm eff})k_-^2 - k_-^4}, \quad (14)$$

where $\theta_{\rm eff} = \theta - 2\langle|\psi_s|^2\rangle$ is the effective detuning shifted by the average power of the stationary field. The eigenvalues, Eq. (14), have a similar form to that of the HSS but now with a dependency on the fast time average. The dependence on the round-trip average power is explicit for the plateau states due to fast time inhomogeneity over the round trip such that when $Y$ is equal to $\langle|\psi|^2\rangle$ the eigenvalues of Eq. (14) reduce to the eigenvalues of the HSS and are comparable to the stability eigenvalues of the LLE [17]. The eigenvalues of Eq. (14) predict no instabilities of the higher power plateaus and a Turing instability of the lower power plateau solution starting at the threshold $Y = 1$ present for $\theta - 2\langle|\psi_s|^2\rangle \geqslant 2$. The critical wave number associated with the maximum growth is given by $k_Y^2 = 2(\theta - 2\langle|\psi|^2\rangle - 2Y_-)$. The HSS of the FP also displays a Turing instability starting at the threshold $H = 1$ when $\theta - 2H \geqslant 2$ [10], and it exhibits the critical wave number $k_H^2 = 2(\theta - 4H)$. Generally, the average intensity of the dark plateau solutions is much larger than the lower power HSS,

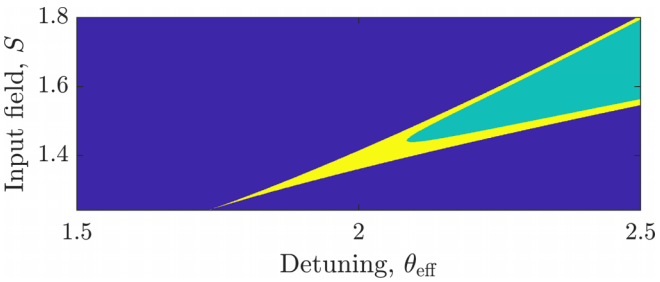


FIG. 2. Stability of coexisting plateaus in the parameter space of shifted detuning, $\theta_{\text{eff}}$, and input field, $S$, for a fixed length of the lower power plateaus $\Delta = 0.2$. The blue regions correspond to single stable HSSs of the FP model, the green regions to two stable plateaus coexisting on the round trip of the resonator, and the yellow region to unstable plateau solutions.

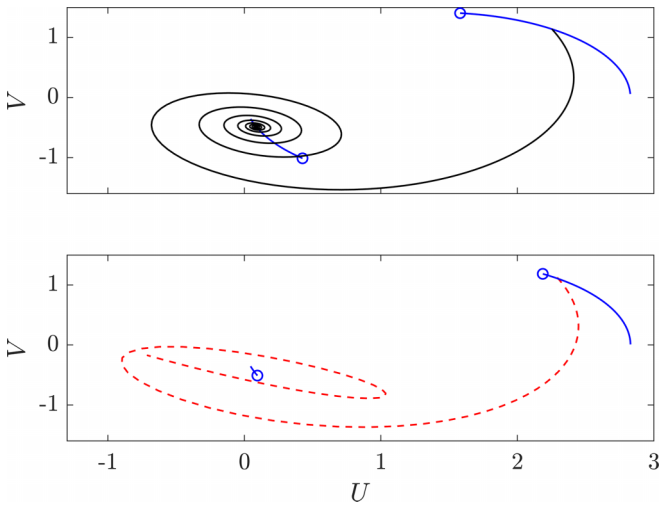


FIG. 3. Examples of SF heteroclinic (black line, top panel) and DCS homoclinic (red dashed line, bottom panel) trajectories in the $V$ vs $U$ plane of Eqs. (8), where $U, V$ are the real and imaginary parts of the intracavity field, respectively. Solid blue lines correspond to upper and lower plateaus of different size $\Delta$. Circles correspond to HSSs.

and as such the critical wave number of the plateau is much smaller than that associated with the HSS, i.e., $k_Y < k_H$.

If we now consider a time-dependent homogeneous perturbation to the plateaus of the form

$$\psi_{\pm} = \psi_{\pm,\text{s}} + \epsilon'_{\pm}(t), \tag{15}$$

we can investigate the linear stability of the plateau solutions to perturbations that change the average power of the field in the slow time $\partial^2_\zeta \psi = 0$. We derive a Jacobian matrix of the linearized plateau system, as can be seen in Appendix A, and we evaluate the eigenspectrum of this Jacobian matrix numerically.

In Fig. 2 the stability of plateau states to perturbations of the average power is reported in the parameter space $(\theta_{\text{eff}}, S)$ when the lower power plateau has size $\Delta = 0.2$. This allows for a direct comparison with the solutions of bistable HSS as seen for a ring resonator [17]. We find that near the onset of optical bistability, plateau solutions in the FP configuration are unstable, as depicted by the yellow zone of Fig. 2. The green zone shows stable plateaus, and the blue indicates solutions of a single stable HSS. We find parameter regimes in which there is a bistability of the HSS of the FP model, but there are no stable solutions of coexisting plateaus. In regions where plateau solutions are unstable, the system cannot support exponentially localized structures which approach them, such as switching fronts (see the next section), and indeed we do not observe the formation of stable dark cavity solitons in this regime.

## IV. SWITCHING FRONTS AND THEIR DYNAMICS

In the previous section, we have studied the existence and stability of plateau solutions connected with a step function. These are approximations to the solutions of Eq. (8) that approach flat solutions along the fast time variable $\zeta$. There are two kinds of such solutions: heteroclinic orbits, i.e., trajectories that connect two separate fixed points of Eq. (8), and homoclinic orbits corresponding to a trajectory that leaves and returns to the same fixed point of Eq. (8). The former corresponds to switching front (SF) solutions while the latter are associated here with cavity solitons: bright (dark) cavity solitons in the case when the fixed point corresponds to the high (low) power plateau. As the boundary conditions of a FP resonator are periodic, SF solutions exist as pairs with opposite orientation in the cavity. Taken together, they form a heteroclinic cycle. DCS solutions described later in this paper are themselves composed of oppositely oriented SFs which interact and lock with each other through local oscillations close to the lower power fixed point, as was first proposed for spatial solitons composed of diffractive switching fronts [31–33]. An example of SF (heteroclinic) and DCS (homoclinic) in the $(U, V)$ plane are presented in Fig. 3. These trajectories are anchored to the plateau solutions discussed in Sec. III for a given value of the distance $\Delta$. The blue solid lines in Fig. 3 correspond to the family of plateau solutions when changing $\Delta$ while the circles mark the positions of the HSS.

We now discuss the stationary states and dynamics of SF (heteroclinic) solutions found for the FP model, and we make a comparison with similar solutions found in ring resonators. The HSSs of the FP model are plotted in Fig. 4(a) as blue curves. The HSSs of an equivalent ring-resonator model are plotted as green curves. When compared with the case of a single field in a ring resonator, it becomes clear that the effect of the shift in the detuning is most prominent for high power solutions, resulting in a large shift of the peak resonance. SF solutions of Eq. (1) present as oppositely oriented pairs and are generally dynamical, moving with identical speed in opposite directions. The velocity of SF solutions depends on the average power of the fields and can display a turning point where the velocities of both SFs change sign. An example evolution is shown in Fig. 5 for fixed parameters from an initial condition near a velocity turning point at $\Delta \approx 0.5$. In the top (bottom) panel of Fig. 5, the SF initial condition has separation slightly narrower (wider) than at the velocity turning point. We can see that the SF solutions either move towards each other until they annihilate (top panel), or move away from each other until the effective detuning is shifted

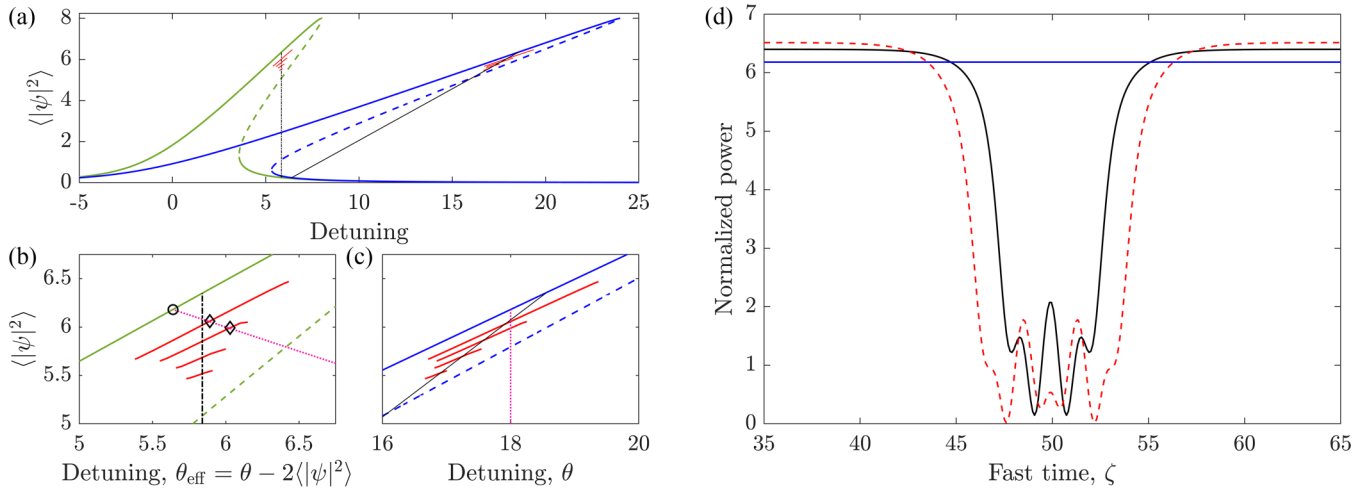


FIG. 4. (a) Solutions of the Fabry-Pérot model and equivalent ring-resonator model for input field $S = 2\sqrt{2}$ with FP length $2L = 100$ and ring circumference $L = 100$. HSSs of the FP (ring-resonator) model correspond to blue (green) lines. Dashed curves correspond to unstable HSSs. Stationary SF solutions are plotted by using their round-trip average power for the FP model (black line) and for the ring-resonator model (black dot-dashed line). Stable dark soliton solutions of different size correspond to the red lines and form branches of distinct width. (b) Solutions of the ring-resonator model plotted with respect to the ring-resonator detuning $\theta_{\rm eff}$, which are related to the FP solutions through the effective detuning, Eq. (7), and corresponding to a zoom of window (a). (c) Solutions of the FP model plotted with respect to the detuning and corresponding to a zoom of window (a). (d) Power profile of bistable stationary dark solitons for parameters $S = 2\sqrt{2}$, $\theta = 18$, $2L = 100$ and corresponding to the two diamonds in (b). The solid blue line in (d) corresponds to the highest power HSS marked with a circle in (b).

beyond the bistability region of the equivalent LLE (bottom panel).

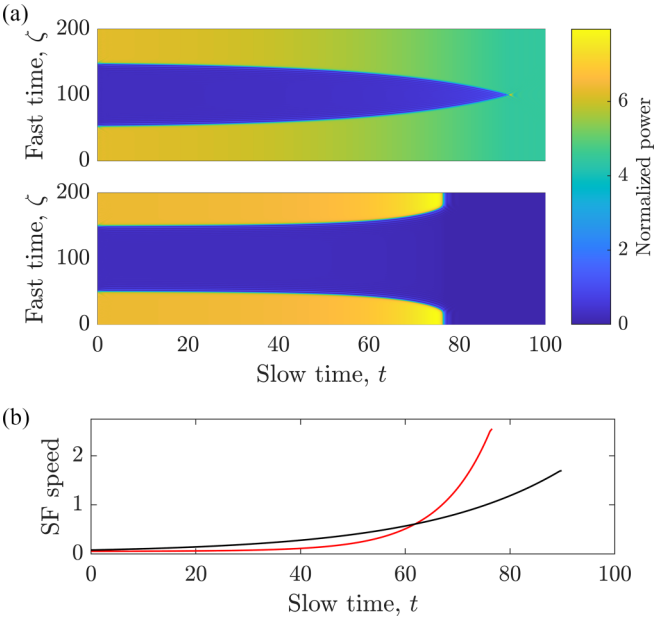


FIG. 5. (a) SFs moving away from the point where their velocity changes direction at a separation of $\Delta \approx 0.5$ for parameters $S = 2\sqrt{2}$, $\theta = 12.5$. The upper panel (lower panel) shows the evolution of two SFs from a square wave initial condition with slightly smaller (larger) SF distance than the turning point. In both cases, the SFs move away from the starting location, annihilate each other, and collapse to one of the bistable HSSs. (b) SF velocities corresponding to the upper panel (black line) and lower panel (red) of (a).

The velocity turning points of the SF of the FP resonator are plotted in Fig. 4(a) as solid black lines, and they correspond to a specific value of $\Delta$ where the effective detuning corresponds to the Maxwell point of the LLE [see the dash-dotted black line in Fig. 4(a)]. The Maxwell point of the LLE corresponds to the unique value of detuning $\Theta_{\rm MP}$ for the chosen parameters where the velocity of a noninteracting SF is zero. This then constitutes a stationary state of the FP model with a value of $\Delta$ providing an effective detuning that is equal to $\Theta_{\rm MP}$. Due to the dependence of the effective detuning on the average power of the field, there exists a single separation of the SF corresponding to a single turning point for the FP. The turning point can then be located semianalytically given that we know $\Theta_{\rm MP}$ as shown, for example, for a bidirectionally pumped ring resonator in [19]. The direction of the SF motion is then determined by the effective detuning being greater than $\Theta_{\rm MP}$ [Fig. 5(a), upper panel] or smaller than $\Theta_{\rm MP}$ [Fig. 5(a), lower panel].

For counterpropagating light in ring resonators, there exists an abundance of stable and robust light plateau stationary states composed of noninteracting SFs that form in one field, while the counterpropagating field is flat in profile [19]. The ring-resonator system is described by two equations with a similar form to Eq. (1), one each for the forward and backward counterpropagating fields. It is interesting to note that for counterpropagation in a ring resonator, the SF with a given initial separation moves towards (instead of away from) the velocity turning point [19]. The difference in direction of SF motion when compared with the FP model is due to distinct backward and forward field profiles present for counterpropagation in ring resonators, such that the effective detuning of each field depends on the power of the counterpropagating field and not explicitly on its own average power. Unlike counterpropagating fields in ring resonators, the stability of

SF solutions in a FP configuration depends critically on its own average power resulting in SF solutions that always move away from the turning point (see Fig. 5). This explains why we do not observe the rich phenomenology of stable SF solutions of the counterpropagation in ring resonators [19] and why only DCSs are achieved through the locking mechanism originating from the interaction of SFs through their oscillating tails, as described in the next section.

Finally, we note that although SF heteroclinic solutions are not stationary in an FP configuration, the calculations of the plateau solutions in Sec. III are still worth mentioning. During the motion displayed in Fig. 5, the solution progresses through the plateau solutions of different size $\Delta$ instant by instant until the two SFs interact with each other. During the SF motion, the cusp point of the heteroclinic trajectory of the top panel of Fig. 3 moves along the blue curves that are the plateau solutions of Eq. (11). If the initial $\Delta$ is larger than that corresponding to the velocity turning point, the cusp of the heteroclinic trajectory on the right-hand side of the top panel of Fig. 3 moves leftward along the blue solid line until it reaches the HSS marked by the circle. If the initial $\Delta$ is smaller than the velocity turning point, the cusp of the heteroclinic trajectory on the right-hand side of the top panel of Fig. 3 moves rightward along the blue solid line until the SFs annihilate and the system collapses to the lower HSS (circle closer to the origin of the axes).

## V. DARK CAVITY SOLITONS

For a FP resonator with normal dispersion, we observe the formation of DCS steady states. Such states are composed of two SFs that lock with each other because of the interaction of fast-time oscillations present close to the lower plateau, as shown for single field ring resonators in [17] and in optical parametric oscillators [32,33]. Bistable DCS stationary solutions of Eq. (1) are shown in Fig. 4(d) for parameter values $S = 2\sqrt{2}$, $\theta = 18$, $2L = 100$. The two dark soliton solutions have different widths corresponding to distinct cycles of the locked oscillatory tails. Such solitons can be obtained by a perturbation of the HSS of suitable width. The results were first obtained through direct numerical integration of Eq. (1) via the Fourier split step method and then verified using lattice relaxation methods.

It can be seen that the plateau power is different from that of the HSS [blue line in Fig. 4(d)] and also for each DCS of different widths. As was discussed in Sec. III, the plateau power of an exponentially localized state depends on the average power of the field over a round trip such that solitons of different width display different plateau power due to their different average power. The DCSs of Fig. 4(d) correspond to the diamonds in Fig. 4(b). The plateau solutions from which a DCS hangs correspond to the points on the solid blue curve of the lower panel of Fig. 3 with the value of the shifted detuning, $\theta_{\text{eff}}$, of the corresponding distance $\Delta$. Note that the bistable DCS and the HSS of the FP model are distributed along the line $\langle|\psi|^2\rangle = -\theta_{\text{eff}}/2 + \theta/2$ as shown in Figs. 4(b) and 4(c) as a pink dotted line, respectively. In agreement with the linear stability of Sec. III, we note that there are no oscillations close to the higher power plateaus and that the oscillations close to the lower power regions correspond to wave vectors $k$ around

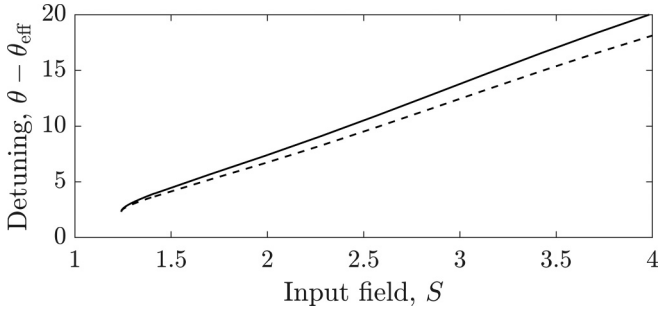


FIG. 6. Approximate difference in detuning between dark soliton solutions of the FP and equivalent ring-resonator models with respect to the common input field. The black line corresponds to the SF turning point when $\Delta = 0$ for the FP model. The dashed line corresponds to the SF turning point when $\Delta = 0.1$.

$2.7 \pm 0.1$, which is far from the Turing wave vector of the HSS of $k_H = 5.99$, as expected, but reasonably close to the predicted $k_Y = 3.3$. The latter discrepancy is due to the fact that the locking of the SFs leads to local deformations of the sinusoidal profiles assumed in the perturbations of Eq. (13). From the predicted value of $k_Y = 3.3$ we can estimate the size $\Delta$ of the two DCSs of Fig. 4(d) to be around 5.7 and 7.6, respectively, in the units used in the figure. These estimates compare reasonably well with the measured values of 6.7 and 8.5.

The effect of the shift in detuning discussed throughout this paper can be understood by making a comparison between the DCS of normal dispersion described here and the FP bright solitons in the anomalous dispersion regime [10]. Due to the large average power of DCS solutions, there is a much larger shift in detuning when compared with the bright solitons in the anomalous dispersion case. DCS solutions are also much further detuned than cavity solitons in an equivalent ring resonator. To see this, we plot in Fig. 6 the difference in detuning values between the FP resonator and an equivalent ring-resonator model $\theta_{\text{eff}}$, and corresponding to the location of a DCS for given input powers $S$. The location of a DCS is approximated by using the SF turning point line [an example of which is shown in Fig. 4(a)] intersecting the high power HSS (solid black line in Fig. 6) or by selecting a point along this line corresponding to a specific DCS size $\Delta$. The dashed black line in Fig. 6 shows solutions in which SFs are stationary with separation $\Delta = 0.1$, the approximate size of the DCS of Fig. 4(d). These lines were calculated using the numerical fit of the Maxwell point of the ring resonator model from Ref. [19]. We see that as the input power is increased, the shift becomes larger. Furthermore, the range of detunings where DCSs exist is much larger for the FP model when compared to an equivalent ring-resonator system. For example, the longest DCS solution branch for an FP resonator spans $16.75 < \theta < 19.37$, see Fig. 4(c), while DCSs in the equivalent ring-resonator system are present only in the range $5.38 < \theta_{\text{eff}} < 6.43$, approximately 2.5 times smaller. The average power of the field is also affected by the number of solitons present in the cavity such that the existence and stability of the solitons depend also on the number of solitons in the cavity. Figure 7(a) shows two bistable DCS solutions

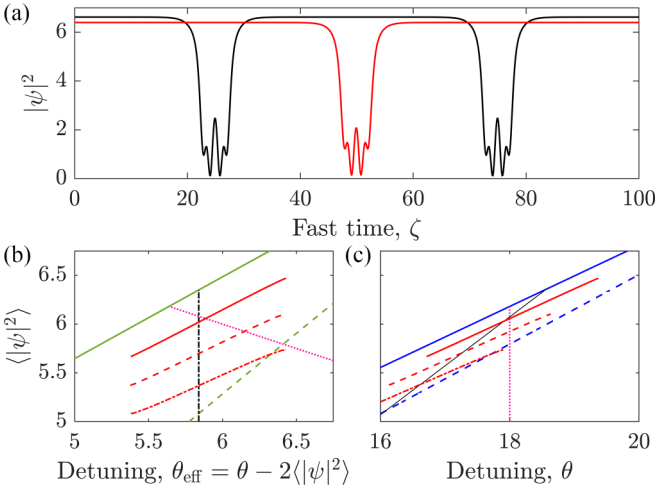


FIG. 7. (a) Soliton states containing a single soliton (red line) and two solitons (black line) for $S = 2\sqrt{2}, \theta = 18$. (b), (c) FP solutions plotted over detuning (or shifted detuning) with respect to their average power. HSSs are plotted as blue (b) and green (c), the black curves correspond to the SF turning point, and dark soliton solutions are plotted as red curves of one (solid line), two (dashed line), and three (dot-dashed line) solitons present in the cavity. The pink dotted line corresponds to the solutions with $\theta = 18$.

for $S = 2\sqrt{2}, \theta = 18$ corresponding to one or two solitons in the cavity. We see that the presence of an additional soliton modifies the low power oscillations and the plateau power. In Figs. 7(b) and 7(c) we plot the DCS solutions as red curves with one soliton (solid), two solitons (dashed), and three solitons (dot-dashed), present in the cavity with an identical number of fast-time oscillations. With each additional soliton in the cavity, the average power of the field decreases. As such, solution branches containing a large number of solitons appear at lower values of detuning. For detuning $\theta = 18$, input field $S = 2\sqrt{2}$ and $2L = 100$, we find that states of one and two solitons are possible, but that further perturbations of the system will not allow the formation of additional solitons, leading instead to the destruction of preexisting solitons.

## VI. OSCILLATORY DYNAMICS

We now investigate the dynamics of DCS states above a temporal instability of Eq. (1). For the case of a ring resonator, dynamical instabilities of DCS solutions due to Hopf bifurcations result in local oscillations of the soliton [17]. In what follows, we demonstrate the effects of the nonlocal coupling of Eq. (1) on the dynamics of oscillatory soliton solutions.

In Fig. 8(a) we show an example of an oscillatory solution of the FP model with input field $S = 2\sqrt{2}$ and detuning $\theta = 18$. We can see that the temporal dynamics of the system is not confined to the soliton but it extends to an oscillation of the background plateau too. As the soliton moves through its limit cycle, there is a change in the average power of the field. Hence, due to the nonlocal self-interaction term, regions of the cavity far from the soliton exhibit oscillatory dynamics with an identical period to that of the soliton. These oscillations are small due to the small change in average power originating from the oscillation of the soliton. A trace

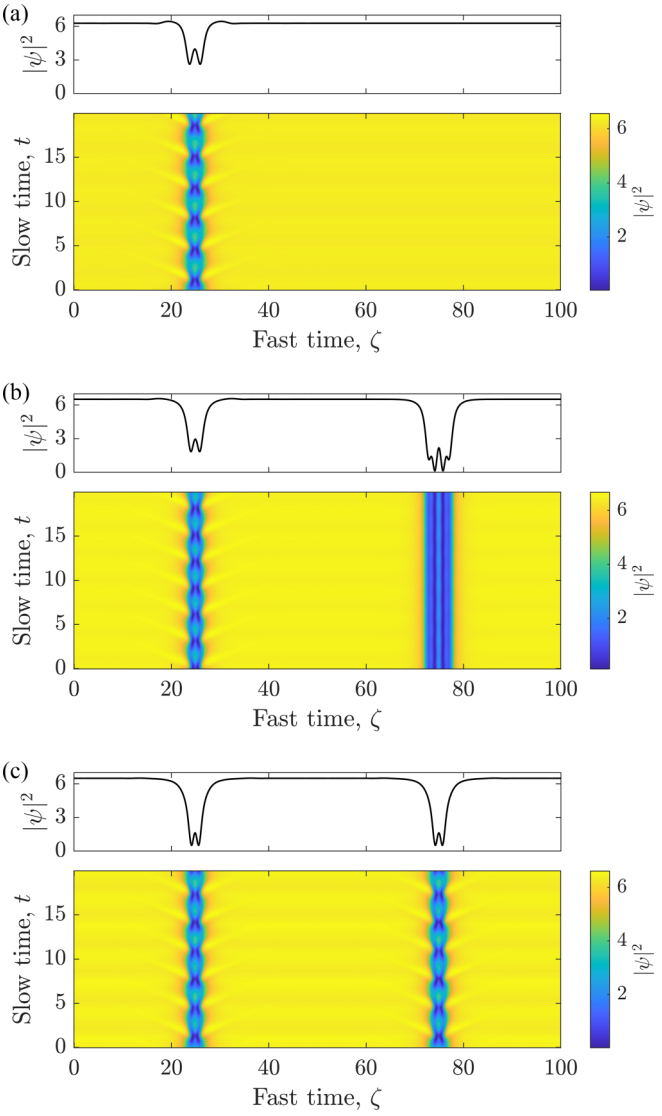


FIG. 8. Oscillating solution with (a) one oscillating soliton, (b) one oscillating soliton and one "stationary" soliton, and (c) two synchronized oscillating solitons (displayed in the upper panels at $t = 20$), all for identical parameters $\theta = 18$, $S = 2\sqrt{2}$. The lower panels display the slow time evolution.

of the minimum power of the oscillating soliton is plotted in Fig. 9(a), showing a single period of oscillation. In Fig. 8(b) we introduce an oscillating dark soliton to an initial stationary solution containing a stable stationary dark soliton shown in Fig. 4(d). The presence of the oscillating soliton induces small temporal oscillations in the plateau power and tiny oscillations in the peaks of the preexistent DCS. The trace of the minimum power is plotted in Fig. 9(b) in black for the oscillating soliton, and in red for the stable soliton. We note that the oscillation period has decreased from Fig. 8(a). In Fig. 8(c), we show the evolution of two synchronized breathing solitons. Here we see a larger oscillation amplitude of the plateau power than in the single soliton case, due to the larger change in the average power of the field resulting from the second oscillating soliton. In Fig. 9(c), we plot the trace of the minimum power of the two oscillating solitons, seen in Fig. 8(c), starting from an

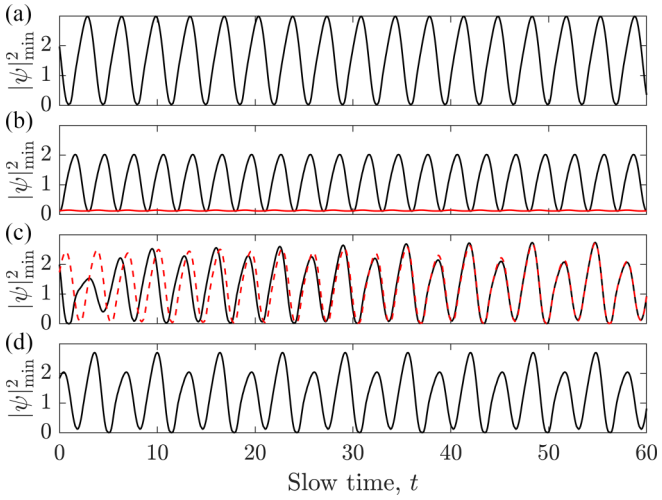


FIG. 9. Oscillating solution with (a) one oscillating soliton in a FP cavity of length $2L = 100$, (b) one oscillating soliton and one locked soliton in a FP cavity of length $2L = 100$, (c) two oscillating solitons in a FP cavity of length $2L = 100$, and (d) one oscillating soliton in a FP cavity of length $2L = 50$, all for identical parameters $\theta = 18$, $S = 2\sqrt{2}$.

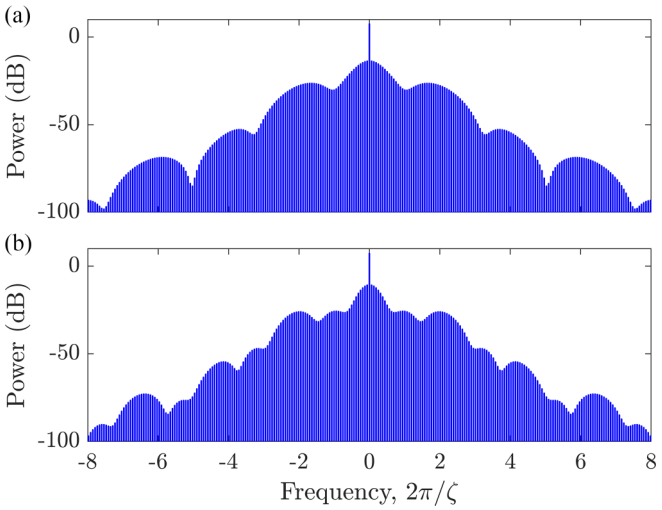


FIG. 10. Bistable frequency combs for parameter $S = 2\sqrt{2}$, $\theta = 18$, $2L = 100$. These spectra correspond to the dark solitons shown in Fig. 4(d) with lesser (a) and greater (b) width.

unsynchronized initial condition. As the system evolves over slow time, the soliton phases begin to overlap, resulting in full synchronization. The resulting dynamics has now experienced a period doubling with respect to the single oscillating soliton. In Fig. 9(d), we plot the evolution of a single soliton with half the cavity length, $2L = 50$, of the previous examples. We see that the dynamics of this single soliton is identical to the synchronized dynamics of the two soliton examples with $2L = 100$ of Figs. 8(c) and 9(c). In general, we find that the dynamics of $N$ well-separated solitons in a cavity of length $L$ synchronizes towards the dynamics of a single soliton in a cavity of length $L/N$.

We find that well-separated solitons, located such that they do not interact through the local dynamics at the tails, experience phase-dependent interaction through the nonlocal coupling. We note that oscillating solitons of the normally dispersive LLE interact locally through their tails and as such do not exhibit synchronization when well separated in a long cavity [17]. In the FP model, the change in average power of the field during an oscillation of a single oscillating soliton is small, and as such the change in the power of the background plateau is also small. By increasing the length of the FP cavity, we can reduce the effects of soliton oscillation on the average power such that we can approach the LLE dynamical and independent solutions. The dynamics of the FP model is most distinct from the ring-resonator LLE when the cavity length is small or the number of oscillating solitons is large displaying long-range interactions leading to synchronization.

## VII. CONCLUSIONS

We have presented bistability, plateaus, switching fronts, and dark soliton states in a Fabry-Pérot model with normal dispersion. Through the use of effective detuning, we demonstrated analogies and differences of these solutions with the stationary states of the ring-resonator case, i.e., the LLE. The homogeneous stationary states of the Fabry-Pérot model have a one-to-one correspondence to the stationary states of a ring resonator described by the LLE, with identical input field and a detuning that is shifted by the average power of the intracavity field over a single round trip. We investigated the linear stability of solutions formed by two plateaus that are different from the homogeneous stationary states and connected by step functions. We identified a region of instability near the onset of optical bistability of the homogeneous stationary states. When compared with counterpropagating light in a ring resonator [19], it turns out that plateau solutions in a Fabry-Pérot cavity with normal dispersion are generally unstable. Their stability analysis, however, is still useful since we can find Turing instabilities of the low power plateaus and determine their critical wave number. Such a wave number is much smaller than those corresponding to Turing instabilities of the homogeneous stationary state. It is this wave number that rules the local oscillations close to the lower plateau when two switching fronts lock to form a stable dark soliton. Due to the shift in detuning, a peculiar feature of dark soliton solutions in the Fabry-Pérot model is that they do not connect to the homogeneous stationary states (as they do in the ring-resonator model), but instead to plateau solutions, which are dependent on the size (average power) of the soliton.

For normal dispersion, the average power of the field, and hence the shift in detuning, is comparatively large for dark solitons when compared with the bright solitons of the anomalous dispersion case. The large shift results in the dark soliton solution branches becoming elongated, occupying a larger domain of detuning values than an equivalent ring-resonator configuration, and found in strongly detuned regimes.

Finally, we investigated the effects of nonlocal coupling on the dynamics of oscillatory solitons. We find that the nonlocal coupling induces temporal oscillations to the homogeneous background power. In the presence of two oscillating solitons, we observe phase-dependent interaction, resulting in synchronization and modifications of their oscillation periods. The resulting synchronized dynamics approach that of

a single soliton with half the cavity length. It was found that the dynamics of the system approached that of an equivalent ring resonator in the limits of a long cavity and small soliton number (small change in average power).

The predictions presented in this paper were obtained for parameter values that are realistically feasible in existing experimental realizations [12]. When these systems operate at normal dispersion, we expect to see the formation of dark soliton steady states in experimental verifications. The Fabry-Pérot system allows for additional design consideration of the cavity properties, allowing for control over frequency comb generation. Example frequency combs of the Fabry-Pérot resonator are shown in Fig. 10, which correspond to the dark solitons of Fig. 4(d) and show distinct modulations on the combs, corresponding to the number of low-intensity fast-time oscillations of the dark soliton [34]. The engineering of frequency combs can be useful in applications in precision spectroscopy, LIDAR, and channel generation for telecom systems.

## ACKNOWLEDGMENTS

This research was supported by funding from the EPSRC DTA Grant No. EP/T517938/1. P.D. acknowledges support by the H2020 European Research Council (ERC) (756966, Counterlight), the Marie Sklodowska-Curie Innovative Training Network (MSCA) (812818, Microcombs), and the Max Planck Society. L.H. acknowledges funding provided by the CNQO group within the Department of Physics at the University of Strathclyde, the "Saltire Emerging Researcher" scheme through SUPA (Scottish University's Physics Alliance) and provided by the Scottish Government and Scottish Funding Council (SFC), and the SALTO funding scheme from the Max-Planck-Gesellschaft.

## APPENDIX

Here we determine the linear stability of plateau solutions in slow time with $\partial_\zeta^2\psi = 0$. We do so by approximating the intracavity field as a step function $\psi = \psi_+ + \psi_-$ composed of higher power $\psi_+$ and lower power $\psi_-$ plateau solutions such that the average power of the field may be written as $\langle|\psi|^2\rangle = \Delta|\psi_-|^2 + (1-\Delta)|\psi_+|^2$, where $\Delta$ is the size of the lower power plateau normalized to the round trip. Hence the higher and lower power plateaus evolve according to the two coupled equations,

$$\partial_t\psi_\pm = S - (1+i\theta)\psi_\pm + i\{|\psi_\pm|^2 + 2[\Delta|\psi_-|^2 + (1-\Delta)|\psi_+|^2]\}\psi_\pm. \tag{A1}$$

The linear stability of the plateau solutions can be understood by finding the eigenspectrum of the Jacobian matrix,

$$J = \begin{pmatrix} -1 - A_+ - 4(1-\Delta)U_+V_+ & B_+ - 4(1-\Delta)V_+^2 & -4\Delta U_-V_+ & -4\Delta V_+V_- \\ -C_+ + 4(1-\Delta)U_+^2 & -1 + A_+ + 4(1-\Delta)U_+V_+ & 4\Delta U_+U_- & 4\Delta U_+V_- \\ -4(1-\Delta)U_+V_- & -4(1-\Delta)V_+V_- & -1 - A_- - 4\Delta U_-V_- & B_- - 4\Delta V_-^2 \\ 4(1-\Delta)U_+U_- & 4(1-\Delta)U_-V_+ & -C_- + 4\Delta U_-^2 & -1 + A_- + 4\Delta U_-V_- \end{pmatrix}, \tag{A2}$$

where $U_\pm, V_\pm$ are the real and imaginary components of the plateaus, and $A_\pm = 2U_\pm V_\pm$, $B_\pm = \theta_{\text{eff}} - U_\pm^2 - 3V_\pm^2$, $C_\pm = \theta_{\text{eff}} - 3U_\pm^2 - V_\pm^2$, where $\theta_{\text{eff}} = \theta - 2\Delta(U_-^2 + V_-^2) - 2(1-\Delta)(U_+^2 + V_+^2)$ is the effective detuning defined in Eq. (7). This formulation allows us to investigate the stability of LLE stationary states for the equivalent FP resonator. Numerical evaluation of the eigenspectrum of Eq. (A2) yields the results shown in Fig. 2 and is discussed in Sec. III.

In the limit $\Delta \to 0$ we can evaluate the eigenvalues of Eq. (A2) as

$$\lambda = -1 \pm \sqrt{A_-^2 - B_-C_-}, \tag{A3}$$

$$\lambda = -1 \pm \sqrt{(A_+ + 4U_+V_+)^2 - (B_+ - 4V_+^2)(C_+ - 4U_+^2)}. \tag{A4}$$

Eigenvalues of Eq. (A3) have a form analogous to the eigenvalues of the homogeneous stationary states of the LLE, and they have a negative real part. The instability of the plateau solutions is therefore due to Eq. (A4).

[1] S. Coen and M. Erkintalo, Temporal cavity solitons in Kerr media, in *Nonlinear Optical Cavity Dynamics: From Microresonators to Fiber Lasers*, edited by P. Grelu (John Wiley & Sons, New York, 2015), pp. 11–40.

[2] A. Pasquazi *et al.*, Micro-combs: A novel generation of optical sources, Phys. Rep. **729**, 1 (2018).

[3] J. Pfeifle *et al.*, Coherent terabit communications with microresonator Kerr frequency combs, Nat. Photon. **8**, 375 (2014).

[4] J. Pfeifle *et al.*, Optimally Coherent Kerr Combs Generated with Crystalline Whispering Gallery Mode Resonators for Ultrahigh Capacity Fiber Communications, Phys. Rev. Lett. **114**, 093902 (2015).

[5] M.-G. Suh *et al.*, Microresonator soliton dual-comb spectroscopy, Science **354**, 600 (2016).

[6] A. Dutt *et al.*, On-chip dual-comb source for spectroscopy, Sci. Adv. **4**, e1701858 (2018).

[7] L. A. Lugiato and R. Lefever, Spatial Dissipative Structures in Passive Optical Systems, Phys. Rev. Lett. **58**, 2209 (1987).
[8] M. Haelterman, S. Trillo, and S. Wabnitz, Dissipative modulation instability in a nonlinear dispersive ring cavity, Opt. Commun. **91**, 401 (1992).
[9] L. A. Lugiato *et al.*, From the Lugiato–Lefever equation to microresonator-based soliton Kerr frequency combs, Philos. Trans. R. Soc. A **376**, 20180113 (2018).
[10] D. C. Cole *et al.*, Theory of Kerr frequency combs in Fabry-Perot resonators, Phys. Rev. A **98**, 013831 (2018).
[11] L. Hill *et al.*, Symmetry broken vectorial Kerr frequency combs for Fabry-Pérot resonators, arXiv:2308.05039 (2023).
[12] T. Wildi *et al.*, Dissipative Kerr solitons in integrated Fabry–Perot microresonators, Optica **10**, 650 (2023).
[13] E. Obrzud, S. Lecomte, and T. Herr, Temporal solitons in microresonators driven by optical pulses, Nat. Photon. **11**, 600 (2017).
[14] T. Bunel, M. Conforti, Z. Ziani, J. Lumeau, A. Moreau, A. Fernandez, O. Llopis, J. Roul, A. M. Perego, K. K. Y. Wong, and A. Mussot, Observation of modulation instability Kerr frequency combs in a fiber Fabry-Pérot resonator, Opt. Lett. **48**, 275 (2023).
[15] K. Y. Yang *et al.*, Broadband dispersion-engineered microresonator on a chip, Nat. Photon. **10**, 316 (2016).
[16] M. Marconi, J. Javaloyes, S. Balle, and M. Giudici, How Lasing Localized Structures Evolve out of Passive Mode Locking, Phys. Rev. Lett. **112**, 223901 (2014).
[17] P. Parra-Rivas *et al.*, Dark solitons in the Lugiato-Lefever equation with normal dispersion, Phys. Rev. A **93**, 063839 (2016).
[18] P. Parra-Rivas *et al.*, Origin and stability of dark pulse Kerr combs in normal dispersion resonators, Opt. Lett. **41**, 2402 (2016).
[19] G. N. Campbell *et al.*, Counterpropagating light in ring resonators: Switching fronts, plateaus, and oscillations, Phys. Rev. A **106**, 043507 (2022).
[20] C. Schelte *et al.*, Tunable Kerr frequency combs and temporal localized states in time-delayed Gires–Tournois interferometers, Opt. Lett. **44**, 4925 (2019).
[21] E. R. Koch *et al.*, Square-wave generation in vertical external-cavity Kerr-Gires-Tournois interferometers, Opt. Lett. **47**, 4343 (2022).
[22] N. M. Kondratiev and V. E. Lobanov, Modulational instability and frequency combs in whispering-gallery-mode microresonators with backscattering, Phys. Rev. A **101**, 013816 (2020).
[23] D. V. Skryabin, Hierarchy of coupled mode and envelope models for bi-directional microresonators with Kerr nonlinearity, OSA Continuum **3**, 1364 (2020).
[24] J. Burke, A. Yochelis, and E. Knobloch, Classification of spatially localized oscillations in periodically forced dissipative systems, SIAM J. Appl. Dyn. Syst. **7**, 651 (2008).
[25] M. Haragus and G. Iooss, *Local Bifurcations, Center Manifolds, and Normal Forms in Infinite-dimensional Dynamical Systems* (Springer, London, 2011).
[26] A. R. Champneys, Homoclinic orbits in reversible systems and their applications in mechanics, fluids and optics, Physica D **112**, 158 (1998).
[27] P. Colet *et al.*, Formation of localized structures in bistable systems through nonlocal spatial coupling. i. general framework, Phys. Rev. E **89**, 012914 (2014).
[28] N. Moroney *et al.*, A Kerr polarization controller, Nat. Commun. **13**, 398 (2022).
[29] W. J. Firth *et al.*, Analytic instability thresholds in folded Kerr resonators of arbitrary finesse, Phys. Rev. A **103**, 023510 (2021).
[30] E. Knobloch, Spatial localization in dissipative systems, Annu. Rev. Condens. Matter Phys. **6**, 325 (2015).
[31] N. N. Rosanov and G. V. Khodova, Diffractive autosolitons in nonlinear interferometers, J. Opt. Soc. Am. B **7**, 1057 (1990).
[32] G.-L. Oppo, A. J. Scroggie, and W. J. Firth, From domain walls to localized structures in degenerate optical parametric oscillators, J. Opt. B **1**, 133 (1999).
[33] G.-L. Oppo, A. J. Scroggie, and W. J. Firth, Characterization, dynamics and stabilization of diffractive domain walls and dark ring cavity solitons in parametric oscillators, Phys. Rev. E **63**, 066209 (2001).
[34] E. Nazemosadat *et al.*, Switching dynamics of dark-pulse Kerr frequency comb states in optical microresonators, Phys. Rev. A **103**, 013513 (2021).